coatings

MDPI

Article

Synthesis of Blue-Emitting $CuAlSe_2$ Quantum Dots and Their Luminescent Properties

Xiaofei Dong [1,*], Xianggao Li [2,*], Shougen Yin [3,*], Jingling Li [4] and Ping Zhang [1]

1 School of Science, Langfang Normal University, Langfang 065000, China; zhangping217@126.com
2 School of Chemical Engineering and Technology, Tianjin University, Tianjin 300350, China
3 School of Materials Science and Engineering, Key Laboratory of Display Materials and Photoelectric Devices, Ministry of Education and Tianjin Key Laboratory for Photoelectric Materials and Devices, Tianjin University of Technology, Tianjin 300384, China
4 School of Materials Science and Hydrogen Energy, Foshan University, Foshan 528000, China; lijl@fosu.edu.cn
* Correspondence: dongxiaofei@tju.edu.cn (X.D.); lixianggao@tju.edu.cn (X.L.); sgyin@tjut.edu.cn (S.Y.)

Abstract: Quantum dot light-emitting diodes (QLEDs) have potential application prospects in new-type display fields due to their wide color gamut, high energy efficiency, as well as low-cost mass production. Research on lead-free and cadmium-free blue quantum dots (QDs) is urgently needed for the development of QLED technology. For I-III-VI QDs, multiple luminescent centers generated by imbalanced local charge distribution have a detrimental effect on the emission performance. Regulating the chemical composition is one of the effective methods to control the defect type of blue-emitting QDs. In this work, narrow-bandwidth (with a full width at half maximum of 53 nm) blue $CuAlSe_2$ QDs are achieved by altering the Cu/Al ratio. As the Cu/Al ratio increases from 0.2 to 1, the photoluminescence (PL) emission peak is red-shifted from 450 to 460 nm, with PL quantum yield up to 56%. The PL spectra are deconvoluted into three emission peaks by Gaussian fitting analysis, demonstrating the main luminescent contribution coming from the radiative recombination of electrons residing in the aluminum–copper antisite (Al_{Cu}) defect level with the holes in the valence band. This work provides a new approach for preparing eco-friendly and high-efficient blue-emitting QDs.

Keywords: I-III-VI quantum dots; blue-emitting; luminescent properties

Citation: Dong, X.; Li, X.; Yin, S.; Li, J.; Zhang, P. Synthesis of Blue-Emitting $CuAlSe_2$ Quantum Dots and Their Luminescent Properties. *Coatings* **2024**, *14*, 1291. https://doi.org/10.3390/coatings14101291

Academic Editor: Fabien Bénédic

Received: 17 September 2024
Revised: 2 October 2024
Accepted: 7 October 2024
Published: 10 October 2024

1. Introduction

Semiconductor quantum dots (QDs) have served as potential emitters for optoelectronic devices [1,2] owing to their remarkable properties, including tunable band gap, high color purity, and solution processability. In the application of QD light-emitting diodes (QLEDs), significant progresses in luminescent efficiency and stability for green- and red-emitting QLEDs [3–5] have been obtained by modulating the nanostructure and band gap of QDs and optimizing the device structure. However, the luminescence performance of blue QLEDs needs further improvement [6–8]. The color purity and efficiency of QDs are the key features for the development of high-efficient QLEDs, in which the relatively mature QD types include group IV [9,10], II-VI [11–13], III-V [14,15], I-III-VI [16,17], and lead-free perovskite QDs [18,19]. The photoluminescence (PL) emission of the above QDs stems from the recombination luminescence induced by excitons and defect states [20,21], thus yielding size/composition-dependent tunable emission ranging from blue to red. Among them, eco-friendly I-III-VI QDs become an attractive emitter suitable for QLEDs owing to excellent absorption and high-stable properties, which have been proven to achieve blue emission in the range of 455 to 475 nm but possess a wide full width at half maximum (FWHM) characteristic from 50 to 90 nm that impairing the color purity for QLED display applications.

The luminescent properties of lead-free and cadmium-free blue-emitting QDs are strongly dependent on chemical composition, size distribution, and energy level structure [22,23]. Kim et al. [16] reported the synthesis of Ag-Ga-S QDs upon introducing Zn^{2+}

ions, exhibiting blue emission at 450 nm with an FWHM of 85 nm, which resulted from the nonexcitonic recombination at intragap states (e.g., Ag vacancy) (V_{Ag}). This work proposed that a V_{Ag} level could be energetically positioned more distantly from the vanlance band maximum, improving the conduction band to V_{Ag} radiative recombination. Bai et al. [22] realized narrow-bandwidth (PL FWHM of 63 nm) blue-emitting $AgGaS_2$/ZnS QDs at 460 nm with a PL quantum yield (QY) of up to 21%, which exhibited a tunable band gap from 2.98 to 2.83 eV by changing the Ag/Ga molar ratio. Xie et al. [17] synthesized Ag-Ga-Zn-S QDs with a facile one-pot approach by varying Ag/Zn and Ag/Ga ratios, in which QDs emitted 470 nm peaking with PL QY of 16.7%. Further, this work demonstrated narrow-bandwidth (electroluminescence FWHM of 53 nm) blue QLEDs based on the QDs, which could be attributed to the improvement of the balance of carrier injection and transport for enhancing device efficiency. At present, developing high-color-purity blue I-III-VI QDs is still a challenge, while PL mechanisms of QDs need further investigation to guide the structural design of QDs for fabricating high-efficient blue QLEDs.

Herein, we presented a facile synthesis of $CuAlSe_2$ QDs by the reverse cation-exchange reaction. The tunable blue-emitting from 450 to 460 nm was achieved by controlling the Cu/Al molar ratio with PL QY up to 56%. X-ray diffraction (XRD) and high-resolution transmission electron microscopy (HRTEM) characterizations were performed to confirm the particle size distribution and phase structure of blue QDs. PL spectra and time-solved PL decay spectra were systematically studied to discuss the photophysical process of QDs. We believe that this work may provide a new approach to synthesizing blue-emitting QDs for new-type QLED applications.

2. Experimental Section

2.1. Materials

Copper acetate ($Cu(OAc)_2$, 99.99%), aluminum isopropoxide ($Al(OCH(CH_3)_2)_3$, 99.998%), indium acetate ($In(OAc)_3$, 99.99%), zinc acetate ($Zn(OAc)_2$, 99.99%), Se powder (99.99%), oleylamine (OLA, 90%), oleic acid (OA, 90%), octadecene (ODE, 90%), dodecanethiol (DDT, 98%), methanol (99.5%), and n-hexane (97%) were purchased from Aldrich Inc (Shanghai, China). All the materials were used without further purification.

2.2. Preparation of Stock Solution

Se powder (0.16 mmol), OA (0.5 mL), ODE (6.0 mL), and DDT (0.5 mL) were mixed in a 100 mL three-neck round-bottomed flask sonicated for 10 min at 25 °C to create Se stock solution, which was then stored at room temperature for future use.

2.3. Synthesis of $CuAlSe_2$ QDs

$Cu(OAc)_2$ (0.16 mmol), $Al(OCH(CH_3)_2)_3$ (0.27 mmol), OA (1.0 mL), ODE (6.0 mL), and OLA (0.5 mL) were first loaded into a 100 mL three-neck round-bottomed flask. The formed mixture was stirred for 10 min under Ar flow, after which it was heated to 120 °C and DDT (0.6 mL) was immediately injected and kept at 120 °C for 15 min until a clear solution was obtained. Afterwards, the temperature was elevated to 200 °C, and the mixture solution was swiftly injected into Se stock solution (1.5 mL) and stirred for 20 min. Subsequently, the reaction system temperature was decreased to 180 °C, following injection into Se stock solution (5.0 mL) and stirred for 15 min to ensure a complete reaction. After 10 s, the mixture was immediately cooled by liquid nitrogen, then the temperature gradually returned to room temperature and a $CuAlSe_2$ QD solution was obtained. The product was precipitated by the addition of excess acetone and purified two times with methanol and n-hexane. The final sample was dispersed into n-hexane for the structural and optical characterization of the QDs. To investigate the luminescence properties of $CuAlSe_2$ QDs, Cu/Al ratios of 0.2, 0.6, and 1 were adopted in the synthetic process with a Cu/Se ratio of 1. $CuInSe_2$ and $CuIn_{0.3}Al_{0.7}Se_2$ QDs were prepared by the identical experimental design.

2.4. Characterization

The crystal structure of all samples was determined by a Rigaku D/max 2500v/pc diffractometer with Cu Kα radiation (Tokyo, Japan). An FEI Talos F200X (Thermo Fisher Scientific, Waltham, MA, USA) operated at an accelerating voltage of 300 kV was used to obtain HRTEM images. PL spectra and decay profiles were measured by a Jobin-Yvon FluoroLog-3 fluorescence spectrometer (Longjumeau, France), using a 450 W Xenon lamp (Tokyo, Japan) and a laser with a wavelength of 376 nm (Tokyo, Japan) as excited sources, respectively. The UV–Vis absorption spectra were recorded on a Hitachi UV-4100 spectrophotometer (Tokyo, Japan). The components of the QDs were characterized by a PerkinElmer ELAN DRC-e inductively coupled plasma mass spectrometer (ICP-MS) (Woodbridge, ON, Canada). PL QY of the QDs was measured by the reference method with rhodamine 6G as a standard reference (95% QY in ethanol) [24]. Cyclic voltammetry (CV) electrochemical measurement (Shanghai, China) of the QDs was carried out in an electrolyte solution of tetrabutylammonium perchlorate (0.1 M) dissolved in dichloromethane. QD film as a working electrode was coated on a glassy carbon electrode, while a platinum wire and Ag/AgCl electrode were utilized as a counter electrode and a reference electrode, respectively.

3. Results and Discussion

3.1. Crystal Structure and Morphology Analysis

The XRD patterns of $CuInSe_2$, $CuIn_{0.3}Al_{0.7}Se_2$, and $CuAlSe_2$ QDs before and after Al^{3+} ion introduction are depicted in Figure 1 to determine the crystal structure of $CuAlSe_2$ QDs. The main diffraction peaks of $CuInSe_2$ QDs located at 26.58°, 44.23°, and 52.39° are ascribed to tetragonal $CuInSe_2$. The diffraction peak position at 19.9° corresponds to the (112) plane of hexagonal κ-In_2Se_3 [25]. After introducing partial Al^{3+} ions, the major diffraction peaks of $CuIn_{0.3}Al_{0.7}Se_2$ QDs are assigned to chalcopyrite $CuAlSe_2$ [26], and the peak positions are obviously shifted towards the higher angles compared to $CuInSe_2$ QDs. The diffraction peaks appearing at 34.28° and 64.60° are matched with the (210) and (411) planes of cubic Cu_2Se. Considering the stable valence state and matching ionic radius, it is reasonable to state that Al^{3+} ions of radius 0.53 Å occupy the sites of In^{3+} ions of radius 0.81 Å in the $CuInSe_2$ QD lattice, inducing the higher-angle shift in diffraction peaks. Moreover, the disappearance of the diffraction peak at 19.9° indicates that the inserting of Al^{3+} ions can suppress the formation of the κ-In_2Se_3 phase. With the complete replacement of In^{3+} ions by Al^{3+} ions, the obtained $CuAlSe_2$ QDs exhibit primary diffraction peaks located at 27.73°, 46.23°, and 54.34°, which are indexed to chalcopyrite $CuAlSe_2$. An increase in the peak intensity of $CuAlSe_2$ QDs was recorded, suggesting an enhancement in the crystallinity of the QDs. The interplanar spacing corresponding to the (112) crystal face in chalcopyrite $CuAlSe_2$ is 0.321 nm.

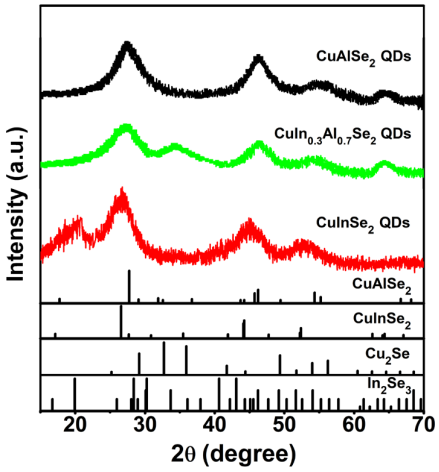

Figure 1. XRD patterns of $CuInSe_2$, $CuIn_{0.3}Al_{0.7}Se_2$, and $CuAlSe_2$ QDs.

To identify the morphology and size of $CuAlSe_2$ QDs with Cu/Al of 0.6, HRTEM measurement was conducted and shown in Figure 2a. The QDs have an almost identical grain size of 4.8 nm, and the crystal place spacing of 0.32 nm is determined by image analysis in Figure 2b, which is assigned to the (112) lattice plane of chalcopyrite $CuAlSe_2$, consistent with the observed XRD result. Further, QDs were digested and then analyzed by ICP-MS to quantify the elemental contents. As shown in Table 1, the actual Cu/Al ratio in the synthesized QDs with a Cu/Al ratio of 0.2 is nearly two times higher than the precursor solution value, which is associated with the difference in the chemical reaction activity among Cu^+, Al^{3+}, and Se^{2-} ions [27]. An enhancement of the actual Cu/Al ratio from 0.41 to 1.16 occurs as the nominal Cu/Al ratio increases from 0.2 to 0.6, accompanied by an increase in the actual Al/(Cu+Al) ratio. This indicates that more Cu^+ ions are replaced by Al^{3+} ions and the content of Al^{3+} ions enhanced from the QD nuclei to the QD surface.

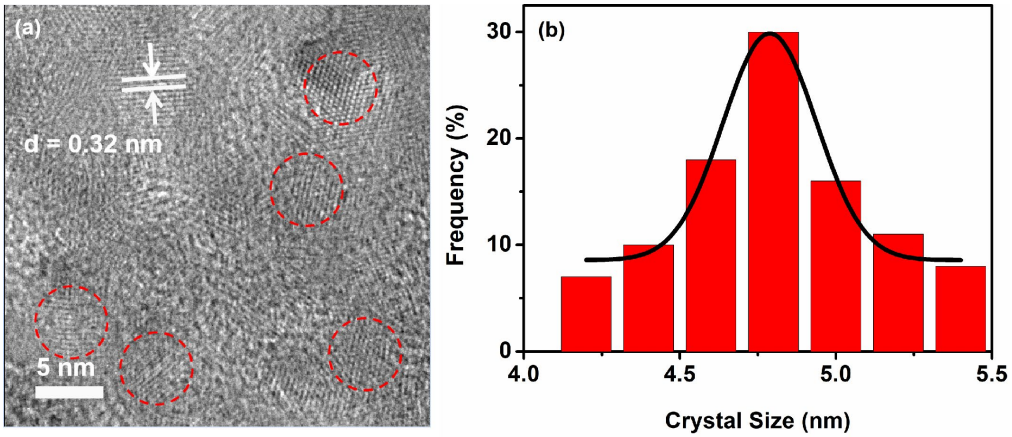

Figure 2. (**a**) HRTEM images; (**b**) the corresponding particle size distribution of representative $CuAlSe_2$ QDs.

Table 1. Nominal Cu/Al ratio and Al/(Cu+Al) ratio in the precursor solution and their actual ratios in synthesized $CuAlSe_2$ QDs determined by ICP-MS.

Precursor Solution Cu/Al Ratio	Precursor Solution Al/(Cu+Al) Ratio	ICP Results of Cu/Al Ratio	ICP Results of Al/(Cu+Al) Ratio
0.2	0.11	0.41	0.20
0.6	0.37	1.16	0.50

3.2. Energy Level and Photoluminescence Analysis

The band gaps of $CuAlSe_2$ QDs with varied Cu/Al ratios were estimated by UV–Vis absorption spectra and CV measurement. As depicted in Figure 3a, a red shift in the absorption onset is observed with an increasing Cu/Al ratio, illustrating that the optical band gap is narrowed from 2.81 to 2.76 eV (Figure 3b) calculated using Tauc's relation [28]. The ionization potential (I_p) and electron affinity (E_a) of QDs with different Cu/Al ratios were calculated using the empirical formula [29]:

$$\begin{aligned} I_P &= -e(E_{1/2(ox)} - E_{1/2(Fc)}) + 4.8)\ \text{eV} \\ E_a &= -e(E_{1/2(red)} - E_{1/2(Fc)}) + 4.8)\ \text{eV} \\ E_g &= I_p - E_a \end{aligned} \quad (1)$$

according to the oxidation onset potential ($E_{1/2(ox)}$) and the reduction onset potential ($E_{1/2(red)}$) (Figure 3c), the edges of the conduction band and valance band were determined and shown in Figure 3d. This result is similar to the research of Lian et al. [30], which illustrated that the obtained $CuInSe_2$/ZnS QDs exhibited tunable band gaps by altering the Cu/In ratio. An enhancement of Cu^+ ions content makes the main contribution for the narrowed band gap and the conduction band slightly downshift of QDs [31,32].

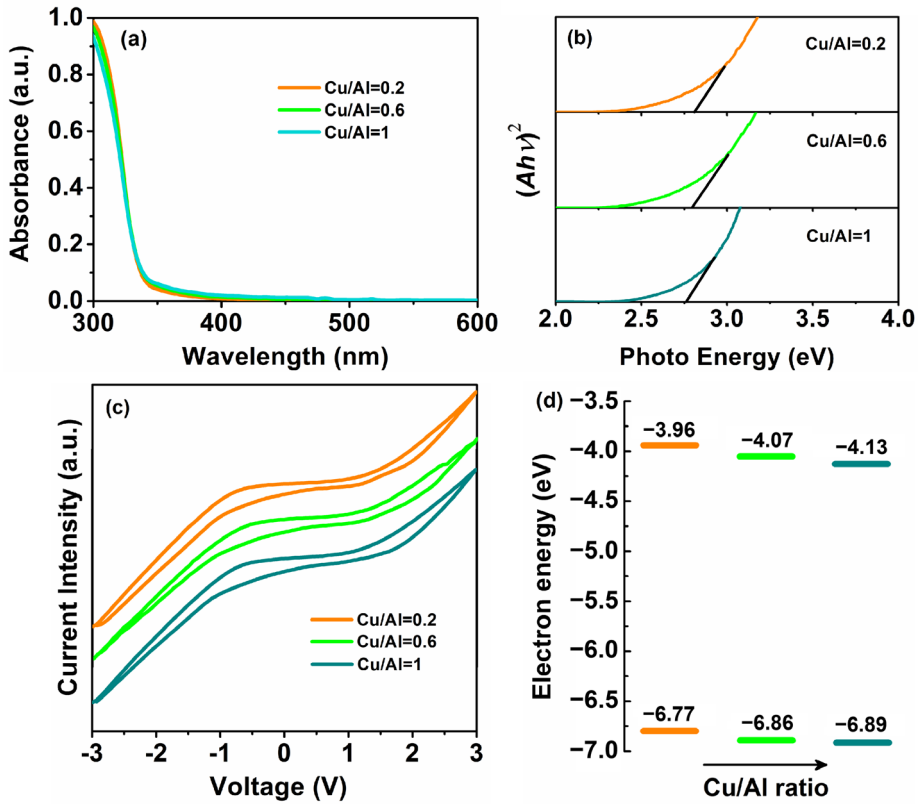

Figure 3. (**a**) UV–Vis absorption spectra of $CuAlSe_2$ QDs with different Cu/Al ratios; (**b**) the corresponding $(Ahv)^2$ (where *A* represents absorbance) dependence on photon energy (*hv*); (**c**) the corresponding CV traces; (**d**) the corresponding energy levels.

The PL spectra of $CuIn_{1-x}Al_xSe_2$ ($0 \leq x \leq 1$) are presented in Figure 4a. It can be seen that $CuIn_{1-x}Al_xSe_2$ (x = 0) QDs exhibit broad-spectrum emission with a PL peak at 645 nm having an FWHM of 107 nm. By introducing some Al^{3+} ions into $CuInSe_2$ QD lattice, the PL spectrum of $CuIn_{1-x}Al_xSe_2$ (x = 0.7) QDs consists of two emission peaks, one at 458 nm and the other at 762 nm, with a weakened emission intensity compared to $CuIn_{1-x}Al_xSe_2$ (x = 0) QDs. From the XRD results in Figure 1, the crystal phase of $CuIn_{1-x}Al_xSe_2$ (x = 0.7) QDs contains both chalcopyrite $CuAlSe_2$ and cubic Cu_2Se structures. It can be concluded that the effect of the exciton transition from cubic Cu_2Se phase (E_g = 2.23 eV) [33] on the total emission in the PL spectrum of $CuIn_{1-x}Al_xSe_2$ (x = 0) QDs could be excluded. In considering the band gap of bulk $CuAlSe_2$ (E_g = 2.7 eV) [34], the narrow spectral emission at 458 nm is related to the band-edge transitions of $CuAlSe_2$ QDs [35]. According to the results reported by Xue et al. [36], aluminum–indium antisite (Al_{In}) defects are easily formed by inserting Al^{3+} ions into the $CuInSe_2$ lattice. It is reasonable to state that the emission at 762 nm is considered to be a composite luminescence of aluminum-related defects (e.g., Al_{In}) and the Cu vacancy (V_{Cu}). After $CuIn_{1-x}Al_xSe_2$ QDs completely transformed into $CuAlSe_2$ QDs, the PL emission peak exhibits a blue-shift from 458 to 450 nm, with an FWHM of 53 nm. Morever, an enhancement in the emission intensity of $CuAlSe_2$ QDs in comparison with $CuIn_{0.3}Al_{0.7}Se_2$ QDs could be attributed to the increased probability of band-edge transitions.

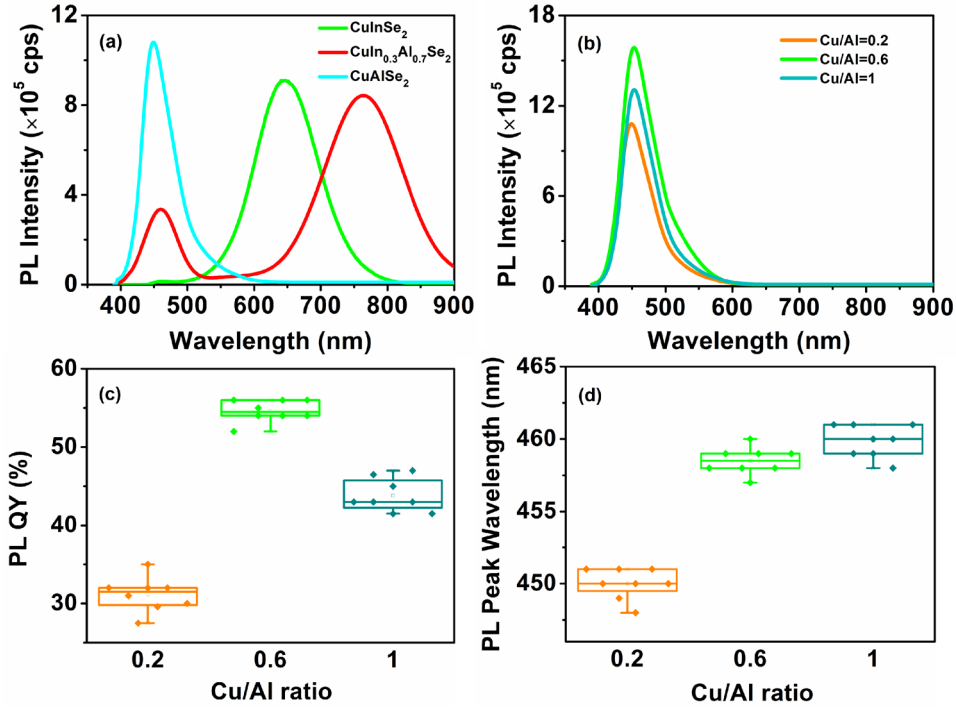

Figure 4. (**a**) PL spectra of $CuIn_{1-x}Al_xSe_2$ ($0 \leq x \leq 1$) QDs monitored at an excitation wavelength of 370 nm; (**b**) PL spectra of $CuAlSe_2$ QDs with different Cu/Al ratios; (**c**) PL quantum yield (PL QY); and (**d**) PL peak wavelength distribution of $CuAlSe_2$ QDs with varied Cu/Al ratios.

3.3. Quantum Yield and Emission Properties

The PL spectra of $CuAlSe_2$ QDs under an excitation wavelength of 370 nm are shown in Figure 4b. With the Cu/Al ratio raised from 0.2 to 1, the maximum PL emission peak is red-shifted from 450 to 460 nm, while the PL QY first increases and then decreases (Figure 4c). At a Cu/Al ratio of 0.6, a maximum PL QY of 56% is achieved. The reproducibilities of PL QY and PL peak wavelength were characterized by the statistics of eight QDs for each batch (Figure 4c,d). The QDs with a Cu/Al ratio of 0.6 exhibit a higher PL QY with the narrow PL peak wavelength distribution than the other two QDs, indicating that the QDs with a Cu/Al ratio of 0.6 possess an improved reproducibility of PL properties. This result is comparable to the previous research that the PL QY of blue-emitting I-III-VI QDs with emission peaks located at 460 to 470 nm is generally less than 50% by using the same reference test [16,23].

Multi-peaks Gaussian fitting makes connections between parameters in the original measurement, and error distribution is utilized to find the emission ratio. Herein, further analysis by Gaussian fitting was performed to investigate the origin of the blue emission. Considering the absorption spectra with a long tail characteristic (Figure 3a) and the PL emission with an FWHM of 53 nm, the PL spectra of $CuAlSe_2$ QDs with different Cu/Al ratios can be easily resolved into three subspectra, which enable the decomposition of the emission with high accuracy, as presented in Figure 5a–c. For $CuAlSe_2$ QDs with a Cu/Al ratio of 0.2, the three fitted emission peaks are located at 443, 460, and 502 nm, respectively. In reference to the findings by Duclaux and co-workers and Baum et al. [37,38], the intrinsic defects in $CuAlSe_2$ QDs include aluminum–copper antisite (Al_{Cu}) donor defects and V_{Cu} acceptor defects. The peak position at 443 nm can be attributed to the transition of electrons from the conduction band to the valence band (CB-VB). The peak centered at 460 nm is associated with the radiative recombination of electrons in the Al_{Cu} defect level with holes trapped in the valence band (Al_{Cu}-VB). The asymmetric broad peak at 502 nm is ascribed to the radiative recombination of electrons in the conduction band to the holes residing in the Cu-related defect band (e.g., V_{Cu}) (CB-V_{Cu}). On the basis of the above multi-peak fitting analysis, the integrated spectral contributions of each emission component are obtained

(Figure 5d). As the Cu/Al ratio increases, the contribution of the radiative transition from Al_{Cu}-VB to the PL spectrum tends to flatten. The CB-VB emissive components for $CuAlSe_2$ QDs with a Cu/Al ratio of 0.6 present a decreasing spectral contribution from 21% to 14%, while Al_{Cu}-VB emission increases from 22% to 30%, indicating a competitive gain between the two radiative transition processes. This result confirms that an enhancement of the Cu/Al ratio induces an increase in the density of V_{Cu} defect states in $CuAlSe_2$ QDs, which supports the variation of PL QY (Figure 4c).

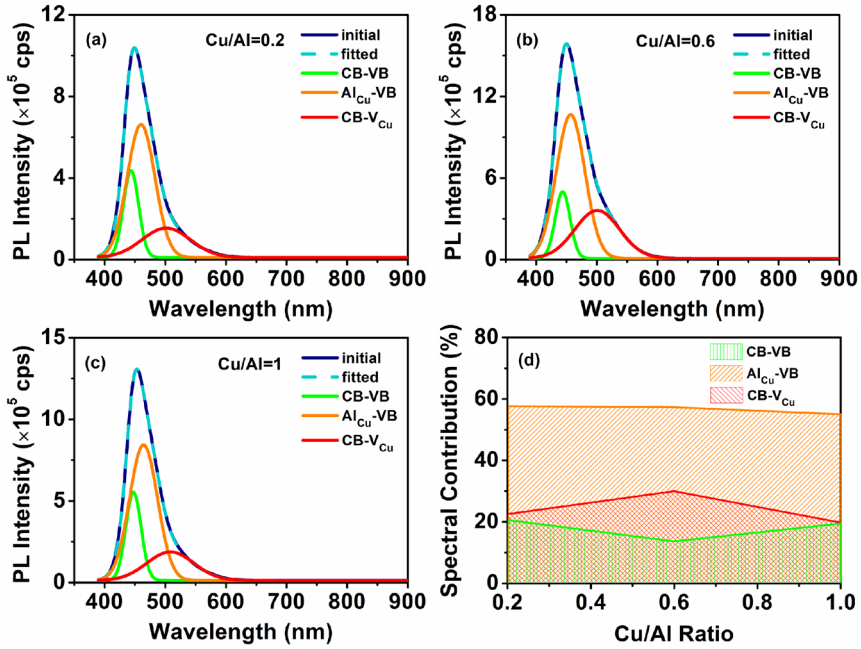

Figure 5. PL spectra resolved into three subspectra: (**a**) Cu/Al ratio: 0.2; (**b**) Cu/Al ratio: 0.6; (**c**) Cu/Al ratio: 1; (**d**) integrated spectral contribution of each emission component.

The representative PL spectra monitored at different excitation wavelengths are to determine the effect of the Cu/Al ratio on the defect levels of $CuAlSe_2$ QDs, as depicted in Figure 6. The PL spectral peak-shape and FWHM of the QDs with the Cu/Al ratio increasing from 0.2 to 0.6 are independent of the excitation wavelength, indicating that the PL emission of $CuAlSe_2$ QDs originates from the identical upper level. For the same sample, the emission peak is red-shifted from 448 to 458 nm as the excitation wavelength increases from 330 to 390 nm, which is caused by the transition of electrons from the shallow donor level to the deep level, and the turning point of the emission peak shift is considered the Al_{Cu} donor level.

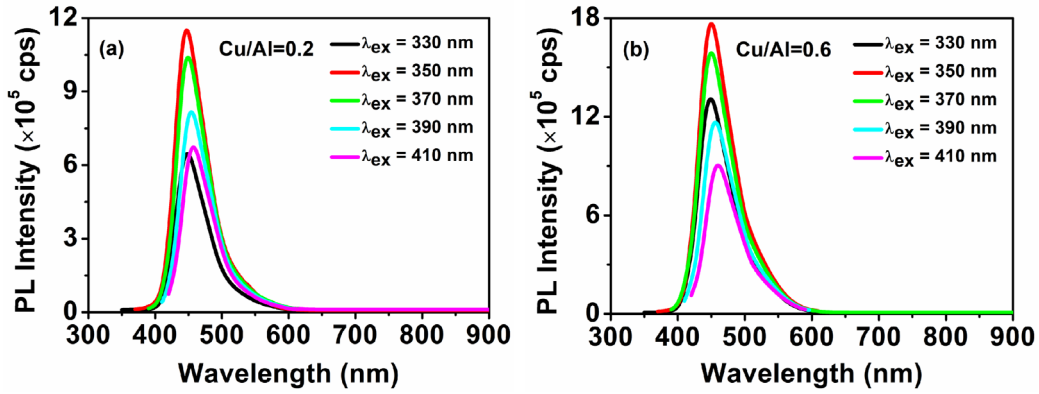

Figure 6. PL spectra monitored at various excitation wavelengths of $CuAlSe_2$ QDs: (**a**) Cu/Al ratio: 0.2; (**b**) Cu/Al ratio: 0.6.

The time-solved PL decay spectra were acquired by monitoring different emission wavelengths to analyze the photophysical process of $CuAlSe_2$ QDs with Cu/Al ratios of 0.2 and 0.6. As presented in Figure 7, the PL decay curves exhibit characteristics that depend on the monitored emission wavelength and the Cu/Al ratio. The curves are well fitted by the following triexponential function [39]:

$$I(t) = A_1 \exp(-t/\tau_1) + A_2 \exp(-t/\tau_2) + A_3 \exp(-t/\tau_3) \quad (2)$$

where τ_1, τ_2, and τ_3 are the decay time constants of PL emission components, and A_1, A_2, and A_3 are the coefficients of decay components of the triple exponential fitting at $t = 0$. The average lifetimes (τ_{av}) were determined according to $\tau_{av} = \sum A_i \tau_i^2 / \sum A_i \tau_i$. It can be seen from the fitting results (Table 2) that with the Cu/Al ratio increased from 0.2 to 0.6, the average lifetime of $CuAlSe_2$ QDs is extended from 235 to 263 ns under 450 nm emission wavelength monitoring, which is consistent with the enhanced PL QY result of QDs. Through fitting calculations, the PL lifetime includes a short lifetime component of τ_1 (1.7 to 3.5 ns), an intermediate lifetime component of τ_2 (32 to 88 ns), and a long lifetime component of τ_3 (205 to 324 ns), which are assigned to the electron transition of CB-VB, Al_{Cu}-VB, and CB-V_{Cu}, respectively. Considering that each lifetime component can reflect the effect of the Cu/Al ratio on the luminescence performance of $CuAlSe_2$ QDs, under same emission wavelength monitoring, the Cu/Al ratio increase is accompanied by the relative decrease in A_1 and A_2 amplitudes and the increase in A_3 amplitudes, indicating that an enhancement of Cu^+ ions content results in an increase in radiative recombination probability from the V_{Cu} defect levels.

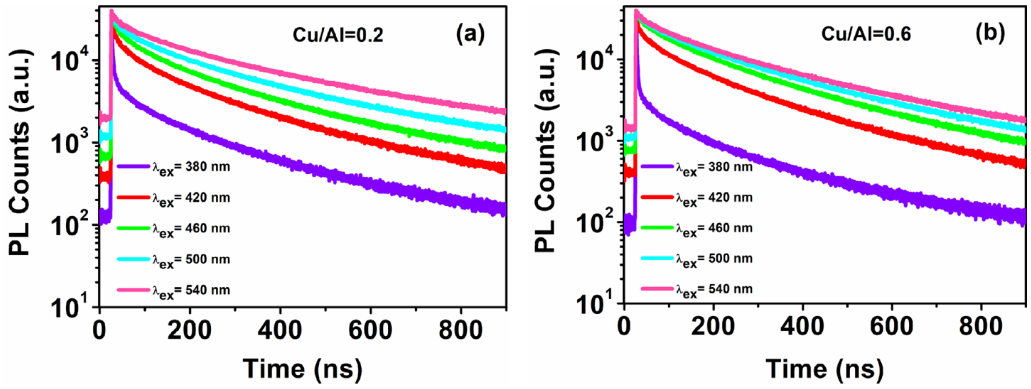

Figure 7. Time-resolved PL decay curves at various emission wavelengths of $CuAlSe_2$ QDs: (**a**) Cu/Al ratio: 0.2; (**b**) Cu/Al ratio: 0.6.

Table 2. Fitting results of PL lifetime decays of $CuAlSe_2$ QDs with Cu/Al ratios of 0.2 and 0.6.

Sample	λ_{em} * (nm)	τ_1 (ns)	A_1 (%)	τ_2 (ns)	A_2 (%)	τ_3 (ns)	A_3 (%)	τ_{av} (ns)
Cu/Al = 0.2	380	1.82	5.97	38.91	19.03	300.29	75.00	192
	420	1.87	5.83	54.82	14.83	218.13	79.34	210
	450	2.26	5.11	65.03	12.25	242.56	82.64	235
	500	2.95	4.21	64.41	11.92	274.57	83.87	267
	540	3.47	3.68	72.29	8.94	314.51	87.38	301
Cu/Al = 0.6	380	1.74	10.16	32.90	14.65	205.86	75.19	199
	420	2.26	5.11	65.03	12.25	242.56	82.64	235
	450	3.01	4.93	76.81	11.09	271.27	83.98	263
	500	3.33	4.43	84.04	10.23	294.51	85.34	286
	540	3.53	3.35	88.07	8.16	324.84	88.49	320

* A monitoring emission wavelength.

4. Conclusions

In this work, blue emission $CuAlSe_2$ QDs were obtained by regulating the Cu/Al ratio. The PL spectra exhibited a red-shift from 450 to 460 nm as the Cu/Al ratio increased from 0.2 to 1, with a maximum PL QY of 56%. The PL spectra were deconvoluted by Gaussian fittings into three emission peaks, while tunable PL emissions were attributed to the competitive radiative transition process from Al_{Cu} and V_{Cu} levels. The PL spectra recorded at various excitation wavelengths presented identical peak-shape and FWHM of QDs, indicating that the blue emission was assigned to the same upper level. Deeper research is needed to optimize the nanostructure of blue-emitting I-III-VI QDs and regulate their energy level for achieving high-efficient QLEDs. This work will provide a new approach toward the development of eco-friendly blue-emitting QD materials and advance the progress in optoelectronic applications, such as new-type QLEDs and solar cells.

Author Contributions: Conceptualization, X.D.; formal analysis, X.D., X.L. and S.Y.; funding acquisition, X.D.; investigation, X.D., J.L. and P.Z.; project administration, X.D. and J.L.; supervision, X.D., X.L. and S.Y.; validation, X.D.; writing—original draft, X.D.; writing—review and editing, X.D., J.L. and P.Z. All authors have read and agreed to the published version of the manuscript.

Funding: This work was financially supported by the Hebei Natural Science Foundation (No. F2022408002), the Science Research Project of Hebei Education Department (No. QN2021122), the Science Research Start-up Funding of Langfang Normal University (No. XBQ202305), and the National Natural Science Foundation of China (No. 51902054).

Institutional Review Board Statement: Not applicable.

Informed Consent Statement: Not applicable.

Data Availability Statement: All data that support the findings of this study are included within this article.

Conflicts of Interest: The authors declare no conflicts of interests.

References

1. Yu, M.; Saeed, M.H.; Zhang, S.; Wei, H.; Gao, Y.; Zou, C.; Zhang, L.; Yang, H. Luminescence enhancement, encapsulation, and patterning of quantum dots toward display applications. *Adv. Funct. Mater.* **2022**, *32*, 2109472. [CrossRef]
2. Mora-Seró, I. Current challenges in the development of quantum dot sensitized solar cells. *Adv. Energy Mater.* **2020**, *10*, 2001774. [CrossRef]
3. Shen, H.; Gao, Q.; Zhang, Y.; Lin, Y.; Lin, Q.; Li, Z.; Chen, L.; Zeng, Z.; Li, X.; Jia, Y.; et al. Visible quantum dot light-emitting diodes with simultaneous high brightness and efficiency. *Nat. Photonics.* **2019**, *13*, 192–197. [CrossRef]
4. Zhang, F.; Cai, B.; Song, J.; Han, B.; Zhang, B.; Zeng, H. Efficient blue perovskite light-emitting diodes boosted by 2D/3D energy cascade channels. *Adv. Funct. Mater.* **2020**, *30*, 2001732. [CrossRef]
5. Li, B.; Lu, M.; Feng, J.; Smowton, P.M.; Sohn, J.I.; Park, I.K.; Zhong, H.; Hou, B. Colloidal quantum dot hybrids: An emerging class of materials for ambient lighting. *J. Mater. Chem. C* **2020**, *8*, 10676–10695. [CrossRef]
6. Hou, D.; Lv, P.; Niu, W.; Guan, Z.; Wang, L.; Zhao, J.; Li, X.; Ye, H.; Tang, A. Controllable synthesis of cadmium-free blue-emitting Cu-Ga-Zn-S-based nanocrystals for solution-processed quantum-dot light-emitting diodes. *J. Phys. Chem. Lett.* **2024**, *15*, 7516–7523. [CrossRef]
7. Zhu, H.; Tong, G.; Li, J.; Xu, E.; Tao, X.; Sheng, Y.; Tang, J.; Jiang, Y. Enriched-bromine surface state for stable sky-blue spectrum perovskite QLEDs with an EQE of 14.6%. *Adv. Mater.* **2022**, *34*, 2205092. [CrossRef]
8. Zheng, Z.; Ren, Z.; Liu, Y.; Yuan, Y.; Zhou, X.; Ji, H.; Shi, H.; Zhang, Y.; Chen, Y.; Zhao, Q. Blue-emitting ZnSeTe/ZnSe/ZnS quantum dots for efficient electroluminescent application. *ACS Appl. Nano Mater.* **2024**, *7*, 13166–13172. [CrossRef]
9. Chen, X.; Han, X.; Zhang, C.; Ou, X.; Liu, X.; Zhang, J.; Liu, W.; Ragauskas, A.J.; Song, X.; Zhang, Z. Synthesis of red, green, and blue carbon quantum dots and construction of multicolor cellulose-based light-emitting diodes. *Small Struct.* **2024**, *5*, 2300449. [CrossRef]
10. Dai, Y.; Xu, W.; Hong, J.; Zheng, Y.; Fan, H.; Zhang, J.; Fei, J.; Zhu, W.; Hong, J. A molecularly imprinted ratiometric fluorescence sensor based on blue/red carbon quantum dots for the visual determination of thiamethoxam. *Biosens. Bioelectron.* **2023**, *238*, 115559. [CrossRef]

11. Han, P.; Li, Y.; Liu, J.; Meng, W.; Zhao, B. High-performance and broad-viewing-angle structural colored films with carbon black and carbon quantum dot doping. *Coatings* **2024**, *14*, 1177. [CrossRef]
12. Lee, S.H.; Song, S.W.; Yoon, S.Y.; Jo, D.Y.; Kim, S.K.; Kim, H.M.; Kim, Y.; Park, S.M.; Yang, H. Heterostructural tailoring of blue ZnSeTe quantum dots toward high-color purity and high-efficiency electroluminescence. *Chem. Eng. J.* **2022**, *429*, 132464. [CrossRef]
13. Cai, W.; Ren, Y.; Huang, Z.; Sun, Q.; Shen, H.; Wang, Y. Emission mechanism of bright and eco-friendly ZnSeTe quantum dots. *Adv. Opt. Mater.* **2024**, *12*, 2301970. [CrossRef]
14. Chen, B.; Li, D.; Wang, F. InP quantum dots: Synthesis and lighting applications. *Small* **2020**, *16*, 2002454. [CrossRef] [PubMed]
15. Huang, F.; Bi, C.; Guo, R.; Zheng, C.; Ning, J.; Tian, J. Synthesis of colloidal blue-emitting InP/ZnS core/shell quantum dots with the assistance of copper cations. *J. Phys. Chem. Lett.* **2019**, *10*, 6720–6726. [CrossRef]
16. Kim, J.H.; Kim, B.Y.; Jang, E.P.; Yoon, S.Y.; Kim, K.H.; Do, Y.R.; Yang, H. Synthesis of widely emission-tunable Ag-Ga-S and its quaternary derivative quantum dots. *Chem. Eng. J.* **2018**, *347*, 791–797. [CrossRef]
17. Xie, X.; Zhao, J.; Lin, O.; Yin, Z.; Li, X.; Zhang, Y.; Tang, A. Narrow-bandwidth blue-emitting Ag-Ga-Zn-S semiconductor nanocrystals for quantum-dot light-emitting diodes. *J. Phys. Chem. Lett.* **2022**, *13*, 11857–11863. [CrossRef]
18. Zhang, J.; Yang, Y.; Deng, H.; Farooq, U.; Yang, X.; Khan, J.; Tang, J.; Song, H. High quantum yield blue emission from lead-free inorganic antimony halide perovskite colloidal quantum dots. *ACS Nano* **2017**, *11*, 9294–9302. [CrossRef]
19. Zhao, J.; Han, B.; Wang, J.; Chen, L.; Xu, L.; Wang, X.; Song, J. Blue lead-free perovskite derivatives: Structural diversity, luminescence properties and light-emitting diode applications. *Adv. Opt. Mater.* **2024**, *12*, 2400277. [CrossRef]
20. Zang, H.; Li, H.; Makarov, N.S.; Velizhanin, K.A.; Wu, K.; Park, Y.S.; Klimov, V.I. Thick-shell $CuInS_2$/ZnS quantum dots with suppressed "blinking" and narrow single-particle emission line widths. *Nano Lett.* **2017**, *17*, 1787–1795. [CrossRef]
21. Dong, X.; Li, X.; Yin, S.; Li, Z.; Li, L.; Li, J. Regulation of photophysical and electronic properties of I-III-VI quantum dots for light-emitting diodes. *Sci. China Mater.* **2024**, *67*, 2734–2748. [CrossRef]
22. Bai, T.; Wang, X.; Dong, Y.; Xing, S.; Shi, Z.; Feng, S. One-pot synthesis of high-quality $AgGaS_2$/ZnS-based photoluminescent nanocrystals with widely tunable band gap. *Inorg. Chem.* **2020**, *59*, 5975–5982. [CrossRef]
23. Jang, E.P.; Han, C.Y.; Lim, S.W.; Jo, J.H.; Jo, D.Y.; Lee, S.H.; Yoon, S.Y.; Yang, H. Synthesis of alloyed ZnSeTe quantum dots as bright, color-pure blue emitters. *ACS Appl. Mater. Inter.* **2019**, *11*, 46062–46069. [CrossRef] [PubMed]
24. Chen, B.; Zhong, H.; Zhang, W.; Tan, Z.; Li, Y.; Yu, C.; Zhai, T.; Bando, Y.; Yang, S.; Zou, B. Highly emissive and color-tunable $CuInS_2$-based colloidal semiconductor nanocrystals: Off-stoichiometry effects and improved electroluminescence performance. *Adv. Funct. Mater.* **2012**, *22*, 2081–2088. [CrossRef]
25. Han, G.; Chen, Z.G.; Drennan, J.; Zou, J. Indium selenides: Structural characteristics, synthesis and their thermoelectric performances. *Small* **2014**, *10*, 2747–2765. [CrossRef]
26. Hergert, F.; Jost, S.; Hock, R.; Purwins, M. Prediction of solid-state reactions for the formation of the chalcopyrites $CuInS_2$, $CuGaS_2$, $CuAlS_2$ and $CuAlSe_2$ starting from binary compounds. *Phys. Status Solidi A* **2006**, *203*, 2598–2602. [CrossRef]
27. Wang, D.; Jin, Z.; Wang, J.; Liu, T.; Li, J.; Lai, J. Wet-chemical synthesis of quaternary chalcopyrite $Cu(In_{1-x}Al_x)Se_2$ nanocrystals by triethylenetetramine-assisted triethylene glycol solution process. *J. Alloy. Compd.* **2014**, *587*, 698–704. [CrossRef]
28. Pervaiz, H.; Khan, Z.S.; Shahzad, N.; Ahmed, N.; Jamil, Q. Synthesis and characterization of $CuInS_2$ nanostructures and their role in solar cell applications. *Mater. Chem. Phys.* **2022**, *290*, 126602. [CrossRef]
29. Wang, P.; Chai, C.; Chuai, Y.; Wang, F.; Chen, X.; Fan, X.; Xu, Y.; Zou, D.; Zhou, Q. Blue light-emitting diodes from mesogen-jacketed polymers containing oxadiazole units. *Polymer* **2007**, *48*, 5889–5895. [CrossRef]
30. Lian, W.; Tu, D.; Weng, X.; Yang, K.; Li, F.; Huang, D.; Zhu, H.; Xie, Z.; Chen, X. Near-infrared nanophosphors based on $CuInSe_2$ quantum dots with near-unity photoluminescence quantum yield for micro-leds applications. *Adv. Mater.* **2024**, *36*, 2311011. [CrossRef]
31. Li, X.P.; Huang, R.J.; Chen, C.; Li, T.; Gao, Y.J. Simultaneous conduction and valence band regulation of indium-based quantum dots for efficient H_2 photogeneration. *Nanomaterials* **2021**, *11*, 1115. [CrossRef] [PubMed]
32. Gong, G.; Liu, Y.; Mao, B.; Tan, L.; Yang, Y.; Shi, W. Ag doping of Zn-In-S quantum dots for photocatalytic hydrogen evolution: Simultaneous bandgap narrowing and carrier lifetime elongation. *Appl. Catal. B-Environ.* **2017**, *216*, 11–19. [CrossRef]
33. Xue, C.; Papadimitriou, D.; Esser, N. Mapping of gradient composition $Cu_xGa_ySe_2$ film properties using Raman and PL-spectroscopy. *J. Phys. D Appl. Phys.* **2004**, *37*, 2267. [CrossRef]
34. Barkat, L.; Morsli, M.; Amory, C.; Marsillac, S.; Khelil, A.; Bernède, J.C. Study on the fabrication of n-type $CuAlSe_2$ thin films. *Thin Solid Films* **2003**, *431*, 99–104. [CrossRef]
35. Harada, Y.; Nakanishi, H.; Chichibu, S.F. Band gap energy bowing and residual strain in $CuAl(S_xSe_{1-x})_2$ chalcopyrite semiconductor epilayers grown by low-pressure metalorganic vapor phase epitaxy. *J. Appl. Phys.* **2002**, *91*, 5909–5914. [CrossRef]
36. Xue, H.; Lu, W.; Zhu, Z.; Tang, F. Al-doped $CuInSe_2$: An ab initio study of structural and electronic properties of a photovoltaic material. *Adv. Mater. Res.* **2012**, *512*, 1543–1547.
37. Duclaux, L.; Donsanti, F.; Vidal, J.; Bouttemy, M.; Schneider, N.; Naghavi, N. Simulation and growing study of Cu-Al-S thin films deposited by atomic layer deposition. *Thin Solid Films* **2015**, *594*, 232–237. [CrossRef]

38. Baum, F.; Pretto, T.; Gouvea, R.A.; Santos, M.J.L. Design of experiments and theoretical investigation for photoluminescence optimization of copper aluminum sulfide nanoparticles through controlling crystalline defects. *Cryst. Growth Des.* **2022**, *22*, 3669–3679. [CrossRef]
39. Zhong, H.; Zhou, Y.; Ye, M.; He, Y.; Ye, J.; He, C.; Yang, C.; Li, Y. Controlled synthesis and optical properties of colloidal ternary chalcogenide $CuInS_2$ nanocrystals. *Chem. Mater.* **2008**, *20*, 6434–6443. [CrossRef]